Tectonics

RESEARCH ARTICLE
10.1029/2019TC005986

Key Points:
- We present a new regional map of Moho topography in the Marmara region, based on RF CCP stacks
- Westward crustal thinning reflects the effect of ongoing extension in western Anatolia and the neighbouring Aegean region
- Abrupt changes in crustal thickness define the non-crustally compensated ancient terrane of the Instanbul block

Supporting Information:
- Supporting Information S1
- Data Set S1
- Data Set S2

Correspondence to:
J. Jenkins,
jj405@cam.ac.uk

Citation:
Jenkins, J., Stephenson, S., Martínez-Garzón, P., Bohnhoff, M., & Nurlu, M. (2020). Crustal thickness variation across the Sea of Marmara region, NW Turkey: A reflection of modern and ancient tectonic processes. *Tectonics*, *39*, e2019TC005986. https://doi.org/10.1029/2019TC005986

Received 14 NOV 2019
Accepted 2 JUN 2020
Accepted article online 8 JUN 2020

Crustal Thickness Variation Across the Sea of Marmara Region, NW Turkey: A Reflection of Modern and Ancient Tectonic Processes

J. Jenkins[1,2], S. N. Stephenson[1], P. Martínez-Garzón[2], M. Bohnhoff[2,3], and M. Nurlu[4]

[1]Department of Earth Science, University of Cambridge, Cambridge, UK, [2]Helmholtz Centre Potsdam, GFZ German Research Centre for Geosciences, Section 4.2: Geomechanics and Scientific Drilling, Potsdam, Germany, [3]Department of Earth Sciences, Freie Universität Berlin, Berlin, Germany, [4]AFAD, Disaster and Emergency Management Authority Turkey, Ankara, Turkey

Abstract The Marmara region in Turkey is an important geological setting, both from a tectonic and a seismic hazard/risk perspective. We present a new map of crustal thickness variation across this complex region to better understand the interplay of past and present tectonic processes that have formed present-day structure. Maps of crustal thickness are created using *Ps* converted phases and receiver function (RF) analysis of earthquakes recorded at all publicly available seismic stations and stations in the national monitoring network (run by AFAD Disaster and Emergency Management Authority Turkey). RFs are converted from time to depth using a local 3-D full-waveform tomographic model and are combined in multiphase common conversion point stacks. Direct *P* to *S* converted arrivals and associated multiples are mapped to produce continuous maps of the Moho discontinuity. Results show Moho depths ranging from 26–41 km with a regional trend of westward thinning reflecting the effects of the extensional regime in western Anatolia and the neighboring Aegean Sea. The thinnest crust is observed beneath the western end of the Sea of Marmara, attributed to transtensional basin opening. A distinct region of increased crustal thickness bounded by the West Black Sea Fault in the west, and the northern strand of the North Anatolian Fault in the south, defines the ancient crustal terrane of the Istanbul Zone. Isostatic arguments indicate that the thickened crust and lower elevation in the Istanbul Zone require it to be underlain by thicker lithosphere, a conclusion that is consistent with its hypothesized origin near the Odessa shelf.

1. Introduction

The structure of the region surrounding the Sea of Marmara in northwestern Turkey is a product of the complex tectonic processes that brought together the multiple crustal fragments that form the modern-day Anatolian plate. The region is also experiencing complex patterns of deformation driven by present-day tectonic processes, from the extensional regime in western Anatolia and the neighboring Aegean region, to the transtensional deformation caused by the major right-lateral strike-slip North Anatolian Fault, which bisects the region. The structure of the crust in this heterogeneous area is likely to be highly variable over short wavelengths, reflecting both ancient and recent tectonic processes.

1.1. Present-Day Tectonic Processes

In eastern Anatolia continental collision of the Arabian and Eurasian plates initiated and potentially still drives the westward lateral motion of the Anatolian plate (Bulut et al., 2012; Şengör et al., 2005; Figure 1a). This motion has been described as either kinematic extrusion of a rigid Anatolian block or as a dynamical flow driven by the differences in gravitational potential energy between the high elevations of Eastern Turkey and the low elevation of the Southern Aegean (England et al., 2016). This westward accelerating motion is also supported by the southward rollback of the Hellenic subduction zone (Bohnhoff et al., 2005; Flerit et al., 2004) and accommodated along the major right-lateral strike-slip boundary delineated by the North Anatolian Fault, leaving central Anatolia relatively undeformed (e.g., Bohnhoff et al., 2016; Le Pichon et al., 2015; Şengör et al., 2005). The Marmara region, which is bisected by the North Anatolian Fault, represents a transition from the undeformed plate center into the N-S extension dominated regime of western Anatolia, which is driven by slab rollback in the Hellenic subduction zone (Faccenna et al.,

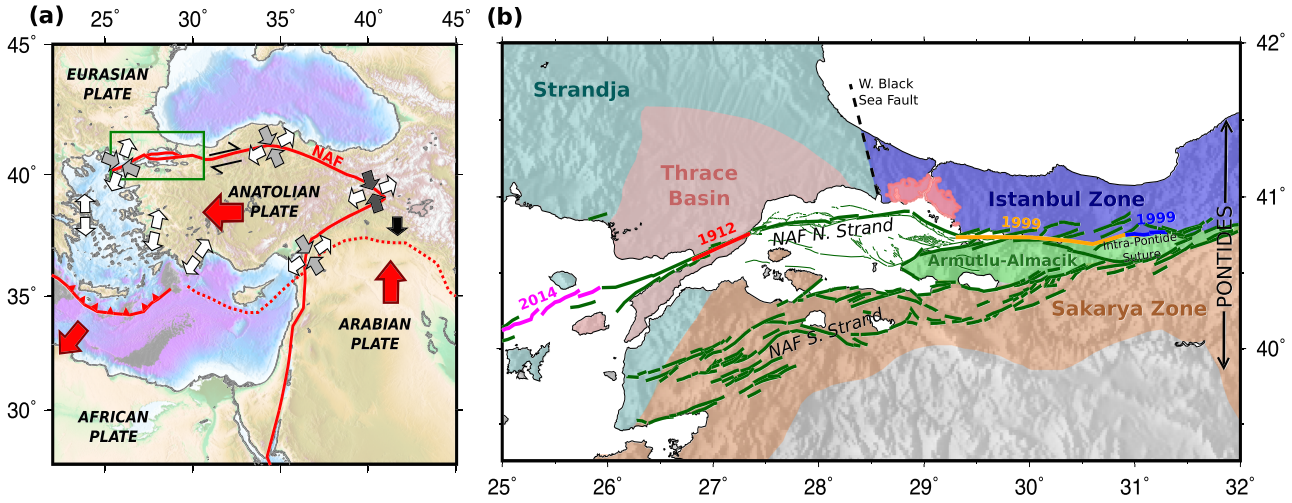

Figure 1. (a) Summarized present-day tectonic configuration of Turkey adapted from Faccenna et al. (2006). Red arrows—plate motion and white/gray arrows—regional stress regime. Marmara region shown in green box. NAF = North Anatolian Fault. (b) Major crustal terranes comprising the Sea of Marmara study region as defined by Okay et al. (1994). Major faults based on Turkey General Directorate of Mineral Research and Exploration (Fatih Bulut, personal communication, 2014) and off-shore faults from Armijo et al. (2005) and Le Pichon et al. (2015). Colored fault segments show major recently ruptured segments with dates.

2006). Interaction of the extensional regime to the west and the strike-slip motion on the North Anatolian Fault creates a transtensional setting in Marmara, as evidenced by the opening of the transtensional basin forming the Sea of Marmara (Le Pichon et al., 2015; Şengör et al., 2005).

Along the majority of its 1,200 km length the North Anatolian Fault comprises a simple single fault strand. However, as it enters the Marmara region it becomes more complex, dividing into at least two main strands —the southern and the northern branch (Figure 1b). To the east of the Sea of Marmara the two branches bound the Armutlu-Almacik crustal block. The northern branch continues westward through the Sea of Marmara, while the southern branch runs to the south becoming a progressively more diffuse fault network.

The majority of slip is thought to be accommodated on the northern branch of the North Anatolian Fault (Barka, 1992; McClusky et al., 2000; Reilinger et al., 2006), which has hosted major >M_W 6.9 earthquakes along much of its length over the last hundred years, apart from the Marmara segment—located just south of the major population center of Istanbul (Bohnhoff et al., 2016). Within the Sea of Marmara, the North Anatolian Fault displays several segments connected with three main basins. Some of these segments, such as the Princes Islands segment directly adjacent to Istanbul, appear to be locked and are hypothesized to be capable of hosting a M>7 event (Bohnhoff et al., 2013; Ergintav et al., 2014). In contrast, parts of the western Marmara segment appear to host creeping sections alternating with locked patches (Bohnhoff et al., 2017; Martínez-Garzón et al., 2019; Wollin et al., 2018).

1.2. Ancient Tectonic Terranes

As well as being subject to a variety of present-day active tectonic regimes, the Marmara region is also a reflection of the ancient tectonic processes that formed it. The region is composed of a series of ancient tectonic terranes of varying origin, some of which still have major effects on present-day deformation processes. For example, the location of the North Anatolian Fault is hypothesized to be controlled by the distribution of ancient crustal terrane fragments (Okay & Tüysüz, 1999).

Anatolia as a single landmass was formed during the closure of the Tethys Ocean, which separated the large continents of Laurussia in the North and Gondwana in the south, at ~350 Ma. Anatolia represents an accumulation of island arcs and continental terranes, which were once distributed throughout the Tethys Ocean. The Marmara region is composed of three of these ancient terranes: Strandja, Istanbul, and Sakarya, collectively known as the Pontides (Okay, 2008) (Figure 1b).

The Intra-Pontide suture zone lies along the northern boundary of the Sakarya terrane, representing the location of continental collision following northward subduction of the Tethys during the Cenozoic Era.

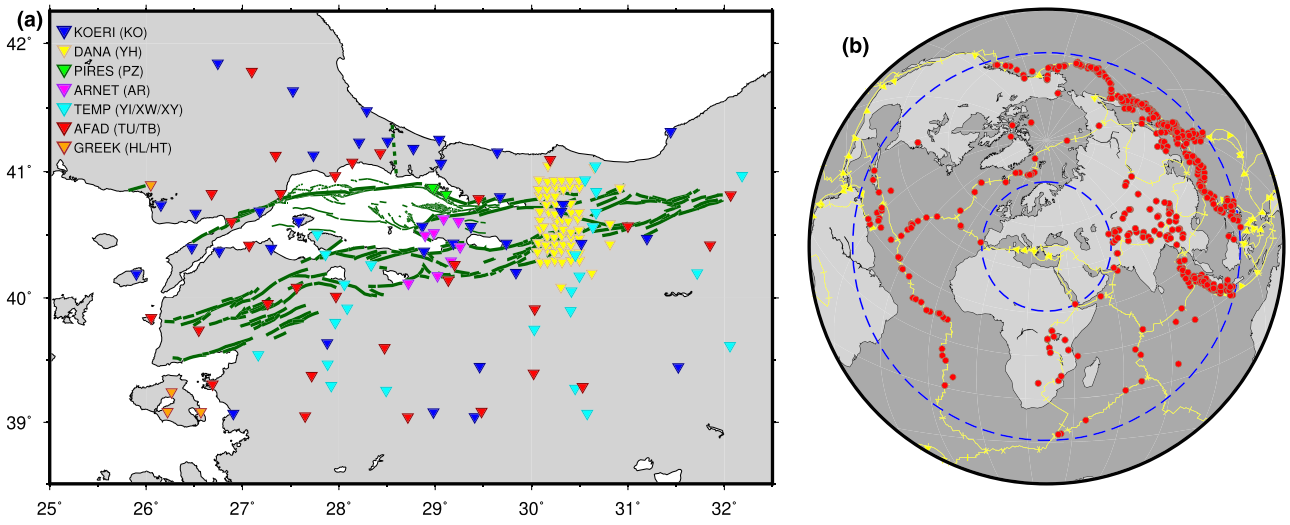

Figure 2. (a) Seismic stations (triangles) used in crustal imaging, colored by network. (b) Distribution of seismic events (red points) used to create RFs. Plate tectonic boundaries of Bird (2003) shown in yellow, with limits of epicentral distance range marked as blue dashed lines at 30 and 90 epicentral degrees.

This 400 km long E-W trending zone now defines the location of the North Anatolian Fault along most of its length (Okay & Tüysüz, 1999).

The Istanbul Zone (IZ) is an elongate east-west oriented block 400 km long and 55 km wide, bounded at its eastern end by the N-S trending fossil transform faults of the West Crimean Fault and at its western end by the West Black Sea Fault (located just west of Istanbul). The IZ is thought to have originally been situated further northward, south of the Odessa shelf (Okay et al., 1994). Onset of back arc spreading in the late Cretaceous period is hypothesized to have caused southward translation of the IZ and the opening of the West Black Sea basin behind it.

To the east of the Sea of Marmara, sandwiched between the IZ and the Sakarya Zone lies the Armutlu-Almacik crustal block. The Armutlu-Almacik block is bounded by transtensional faults, which represent the splitting of the present-day North Anatolian Fault (Bulut et al., 2007; Pucci et al., 2006). It is unclear whether the units comprising this block resemble the Istanbul Terrane, Sakarya Terrane, or a mixture of both (Elmas, 2012; Yiğitbaş et al., 1999), and there are several debated scenarios as to its origin (e.g., Elmas & Yiğitbaş, 2001; Okay & Tüysüz, 1999).

The Strandja massif is a predominantly crystalline terrane that makes up a large part of the southern Balkans. The region to the northwest of the Sea of Marmara is largely covered by the tertiary depression of the Thrace sedimentary basin, which is proposed to be a fore-arc basin linked to closure of an Intra-Pontide Ocean (Görür & Okay, 1996).

1.3. Previous Seismic Observations

Large-scale, country-wide studies of Turkish crustal thickness variation conducted using receiver function (RF) analysis have identified a long-wavelength signal of westward crustal thinning moving from central Anatolia (~35–40 km) into the Marmara region (~28–32 km) (Karabulut et al., 2019; Tezel et al., 2013; Vanacore et al., 2013). This has been interpreted to represent the increasing effect of the extensional regime in the Aegean.

The SEISMARMARA-Leg1 project carried out wide-angle reflection and refraction surveys using on-land and ocean bottom seismometer deployments, to define the crustal structure beneath the Sea of Marmara itself (Bécel et al., 2009). Results show crustal thinning of on the order of 10 km from on-shore to offshore on east-west profiles within the Sea of Marmara to minimum crustal thicknesses of 26 km.

On a much smaller scale, several local studies have made inferences of detailed fault structure using the Dense Array for Northern Anatolia (DANA), located east of the Sea of Marmara straddling the north and south branches of the NAF (Figure 2a DANA stations plotted as yellow triangles). Frederiksen et al.

(2015) used transfer functions to determine crustal thickness across the two fault branches. They observed a step increase in Moho depth across the northern branch of the fault, coincident with the surface expression indicating a steeply dipping fault structure extending to depth. They noted that this increase in Moho depth correlated with a decrease in elevation and hypothesized that the crust in the IZ was not in isostatic equilibrium. The ambient noise autocorrelation study of Taylor et al. (2016) also observed offsets in Moho depth across the northern branch of the fault. Based on disruption in the amplitude of reflected arrivals they also concluded that that both branches of the fault represented narrow shear zones (<10 km) at depth, with the northern branch extending to greater depths than the southern branch. The local RF study of Kahraman et al. (2015) supported the conclusion of narrow fault zones but suggested that the southern fault branch represents a more diffuse structure then the northern branch. Unlike the previous two aforementioned studies, Kahraman et al. (2015) did not observe a significant change in depth across the northern branch of the NAF. They also suggest that both fault branches vary from a near vertical orientation to a 60° northward dipping structure from west to east across the small footprint of the array.

1.4. A New Map of Crustal Thickness Variation Across the Marmara Region

In this study we focus on mapping crustal structure across this evolving area on a regional scale, with the aim of better understanding how the interaction of past and current tectonic processes interact to form present-day crustal structure. Observations of crustal thickness not only aid in understanding tectonic processes but are also important for assessing hazard potential. Variation in crustal thickness has been shown to effect potential event magnitudes (Ben-Zion & Lyakhovsky, 2002; Klinger, 2010). Moho depth variation is also an input parameter in geomechanical modeling, which can be used to determine stress state and hazard potential (Hergert & Heidbach, 2011). Previous modeling in the Marmara region has used compiled point estimates of crustal thickness from a range of studies (Hergert & Heidbach, 2011). These individual studies will have used slightly different techniques and approaches, which have variable lateral sensitivity. Here we produce a new continuous and laterally consistent map of crustal thickness across this region, for use in future modeling studies.

Using a comprehensive seismic data set (Section 2), we make observations of *Ps* converted phases using RF analysis (Section 3.1) to image the seismic Moho. Using multiphase common conversion point (CCP) stacking of our data (Section 3.3), we produce a new regional-scale map of continuous crustal thickness variation across the Marmara region, which we interpret based on both present-day tectonic and ancient crustal structures.

2. Seismic Data

We bring together a comprehensive data set, combining all available broadband seismic stations in the Marmara region (Figure 2a). This data set includes stations from the permanent Turkish AFAD network (Disaster and Emergency Management Authority Turkey), KOERI network (Kandilli Observatory and Earthquake Research Institute, Bosphorus Univ, 2001), PIRES Prince Islands network (Bulut et al., 2009), and a selection of stations from two Greek networks (Aristotle University of Thessaloniki, Seismological Network, 1981; National Observatory Of Athens, I. O. G., 1997). The temporary Dense Array for North Anatolia network (DANA, 2012) provides dense coverage in the west of the region, while stations from the ARNET network (run by GFZ Potsdam in conjunction with the Kocaeli University) increase data coverage over the Armutlu Peninsular (Tunc et al., 2011). We also include data from numerous other small-scale temporary deployments (Paul, 1981, 2007, 2013). This compilation gives a total of 174 seismic stations running at various time intervals between 2006 and 2018, which is an unprecedentedly high number of stations available for this region.

Earthquakes with magnitudes ranging between M_W 5.5–8.0 within 30 to 90 epicentral degrees occurring during the run time of each station were selected for RF analysis (Figure 2b, inset). This distance range limits data to near-vertical incoming raypaths (required for the analysis applied) and avoids regions affected by either phase triplications at closer distances or by interaction with the outer core at greater distances.

3. Theory and Method

3.1. *Ps* Converted Phases

When incoming seismic waves interact with sharp changes in seismic velocity, such as the Moho, energy can be converted between compressional (*P*) and transverse (*S*) waves (Figure 3a). These are referred to as *Ps* phases, where the lower case "s" denotes the upgoing nature of the *S* wave after conversion. Directly following direct *P* wave arrivals, it is possible to observe *Ps* converted phases, from *P* wave energy that is converted to *S* waves at discontinuities beneath the recording station. The delay time between the direct *P* wave and later *Ps* arrivals can be used to estimate the depth of underlying discontinuities. For shallow structures, in addition to direct *Ps* phases, it is important to consider multiples which bounce within seismic layers. Major multiples considered in this study are the positive polarity *PpPs* and the coarriving negative polarity *PpSs* and *PsPs* phases (Figures 3a and 3b).

3.2. Receiver Functions

To highlight Ps arrivals and allow stacking between events with different source time functions, we use Receiver Function (RF) analysis. This method involves deconvolving the effects of instrument response and event source from seismograms, leaving a direct representation of discontinuity structure along the incoming raypath (example shown in Figure 3b). For near-vertical waves we assume that the vertical component of motion is a good approximation of the event source and deconvolve this signal from the radial component of motion, on which *Ps* phases are preferentially recorded. Deconvolution is carried out using the iterative time domain method of Ligorria and Ammon (1999). In this approach RFs are iteratively built in the time domain from Gaussian pulses of a set width. The Gaussian pulse width imposes an implicit frequency filter on seismic data, as periods less than than the Gaussian width will not be resolvable. In this study we generate two sets of RFs built with Gaussian pulses of different width. Variable Gaussian pulse widths are required due to the way data are treated during time-to-depth conversions, as discussed further in Section 3.3. Calculated RFs are then either accepted for further analysis or discarded based on the following quality control criteria:

1. That signal to noise ratio of *P* wave energy compared to the full trace >2 in raw waveform data.
2. The direct *P* wave arrival is the maximum amplitude peak in the RF, with no preceding peaks >30% of this amplitude.
3. When reconvolved with the vertical component, the RF can reproduce the transverse component with at least 60% tolerance. The tolerance represents the percentage of the power of the original trace that is reproduced, defined as

$$Tolerance = \left(1 - \left(\frac{\sum (U_R - (RF * U_Z))^2}{\sum (U_R)^2}\right)\right) * 100 \quad (1)$$

where U_R is the radial component and $(RF * U_Z)$ is a convolution of the RF and the vertical component.

During a final manual quality control check, RFs are discarded if they have anomalous long wavelength features or are significantly different to others that sample the same region.

3.3. Multiphase CCP Stacking

Within individual RFs, Ps arrivals can be within the level of noise; thus, RFs are generally stacked to enhance coherent arrivals and suppress incoherent noise. The stacking methodology used here is described in detail in Jenkins et al. (2018) and summarized below.

We use CCP stacking where each RF is migrated to depth along its incoming raypath within a 3-D grid. We set up a 625 km by 425 km grid across the Marmara region, sampled every 2.5 km laterally and every 0.1 km vertically down to 60 km depth. The RF amplitude is added to all grid points within the ray Fresnel zone, which increases in width with increasing depth as velocities and thus wavelength increases. Amplitudes are given a decreased weighting, *W*, with distance from the raypath to avoid sharp edge effects so that

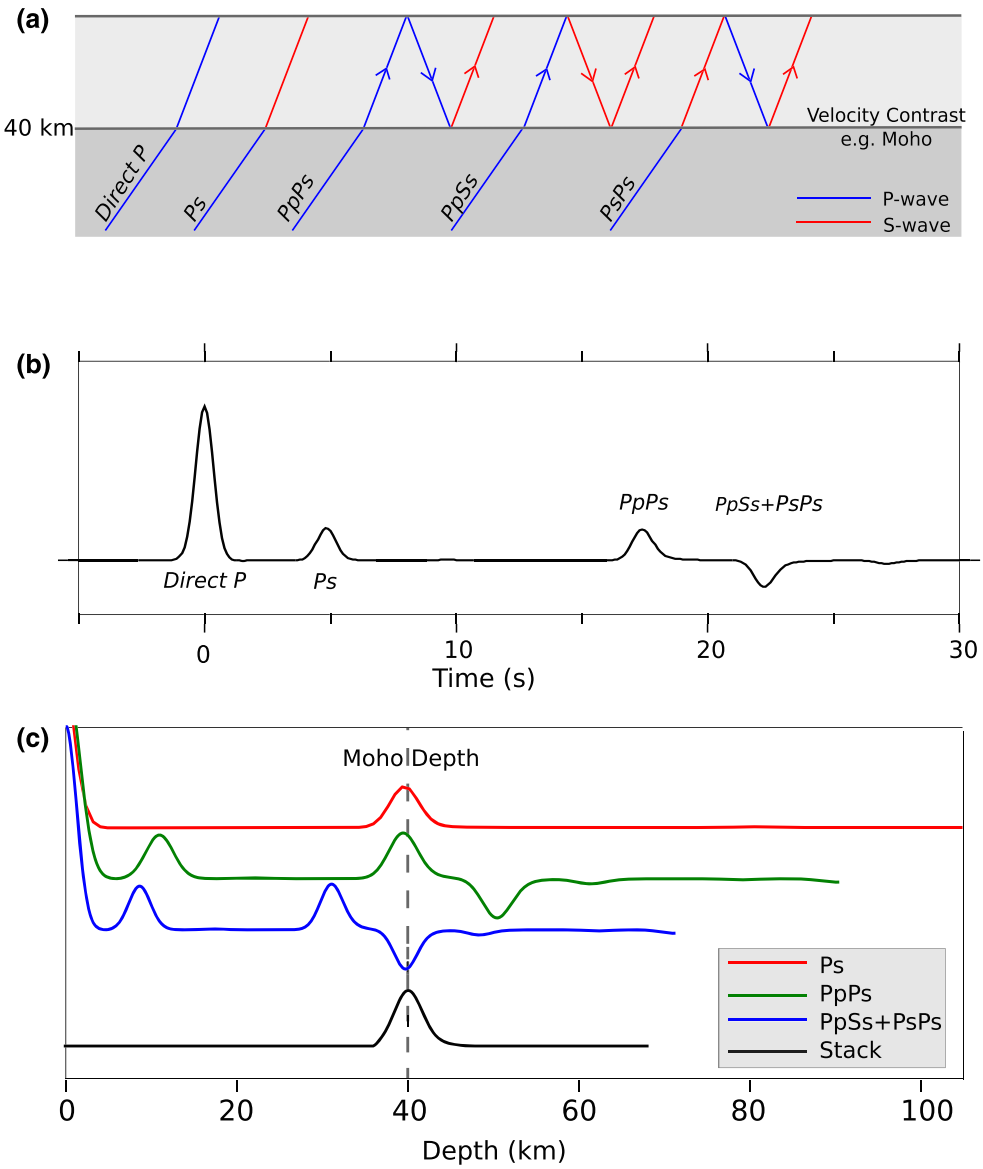

Figure 3. (a) *P to S converted* phases of interest in crustal imaging. (b) Example of a synthetic RF highlighting phases shown in (a). (c) Example of a multiphase time-depth conversion and multiphase stacking procedure.

$$W = \frac{1}{1 + \exp(15 * (\Delta - 2))}, \tag{2}$$

where Δ represents the fresnel zone half width. This technique allows for stacking between closely spaced stations as well as directional variation in observed structure at a single station.

We add data across the Fresnel zone of the ray, as this represents the true area to which data are sensitive, rather than assuming a point measurement at the center of the raypath. We refer to this as the 1 × Fresnel zone stack, which is used to explore the more densely sampled regions to the east of the Sea of Marmara in detail, where closely spaced stations lead to many overlapping raypaths. A second stack is produced where data are added across two Fresnel zones (i.e., 2 × Fresnel zone stack). This stack introduces a degree of data smoothing and lateral interpolation, which we deem justifiable given the similarity of measurements in adjacent areas, which are seen in the 1 × Fresnel zone stack. This procedure enables construction of a broad-scale picture of crustal structure, which we use to interpret regional-scale trends. The effect of

lateral smoothing can be observed by directly comparing 1 and 2 × Fresnel zones stacks and is shown in supporting information Figure S1.

When investigating crustal thickness, shallower structures can produce early arriving *Ps* phases and associated multiples, which complicate the waveform, potentially making identification of Moho *Ps* phases difficult. To avoid the possibility of misinterpreting multiple arrivals as real discontinuity structure, we employ a multiphase stacking technique. This approach involves converting RFs from time to depth three times assuming all peaks represent: (1) direct *Ps* conversions, (2) *PpPs* multiple phases, and (3) *PpSs* multiple phases (Figure 3c). These different time-depth conversions act to stretch RF signals to different extents. Accordingly, to make peaks of equivalent width after time-to-depth conversion, we create two sets of RFs which are built with Gaussian pulses of different width. Set 1 RFs are converted from time to depth assuming phases represent direct *Ps* conversions and are built with Gaussian widths of 0.5 s. Set 2 RFs are converted from time to depth assuming phases represent multiples and are built with Gaussian width of 2 s. Building RFs with Gaussian pulses of these periods is equivalent of low-pass filtering the data at 2 and 0.5 Hz in Sets 1 and 2, respectively. This allows resolution of discontinuities separated by >5 km vertically. A CCP stack is created for each set of time-to-depth converted RFs. Each individual stack will contain some peaks migrated to the incorrect depth. Stacks are then combined only where consistent arrivals are observed across all stacks (Figure 3c), since any true discontinuity structure should produce all three phases. A real data example of this procedure is shown in Figure 4. Peak maxima that are above 2 standard error of the mean and contain >3 stacked RFs are automatically picked throughout the final stack. Discontinuities are then defined based on the depth distribution of automatically picked peaks and identification of clear continuous features in cross sections.

We use the 3-D full waveform tomographic model of Çubuk-Sabuncu et al. (2017) (which contains models of both V_P and V_S variation) to convert RFs from time to depth, accounting for lateral velocity variation across the region. To understand the effects of our 3-D corrections, we compare results to stacks converted to depth using the 1-D velocity model of Karabulut et al. (2011) developed for the eastern Marmara sea region, which is commonly used for regional earthquake location (e.g., Wollin et al., 2018).

We believe that the method outlined here will be superior in defining reliable Moho depth estimates in geologically complex regions compared to more commonly applied RF methods such as HK stacking (Zhu & Kanamori, 2000) or inversion for 1-D structure. HK stacking assumes a constant velocity, single-layered crust, which is likely to lead to inaccuracies in areas of more complex crustal structure (Ogden et al., 2019). Inverting RFs for a model of 1-D velocity structure accounts for more variation. However, RFs alone do not have sensitivity to absolute velocities, due to trade-offs in arrival time between layer thickness and velocity. Accordingly, modeling requires a reasonably accurate starting model or constraints from additional data such as surface wave dispersion measurements to be reliable. Thus, results can be highly dependent on how the model is parameterized. Deciding which point in the resulting velocity profile should be defined as the Moho can also be a somewhat subjective decision. Finally, both of these techniques give point measures of Moho depth at each station, rather than exploring the potential 3-D variation by exploiting arrivals from different back-azimuths. By using CCP stacking and a local high-resolution, 3-D, full-waveform velocity model for time-to-depth conversion, we account for our best current estimates of the 3-D variations of velocity structure in this region. Finally, by using a multiphase stacking approach, we reduce uncertainties in our interpretation of which arrivals in the final image should be interpreted as the Moho.

Figure 4 demonstrates an example where this multiphase approach is useful. Figure 4a shows a stack assuming all arrivals are *Ps* conversions. The majority of the profile shows a clear Moho arrival at approximately 25–30 km depth shown as a dashed line. However, at the eastern edge of the profile two arrivals are observed at ~40 and ~20 km (labeled as Peak 1 and Peak 2, respectively, in Figure 4a), either of which could be interpreted as the Moho. By considering stacks which are time-to-depth converted assuming arrivals represent multiple phases *Pps* and *PpSs* (Figures 4b and 4c), this ambiguity is removed, as it becomes clear that only the deeper Peak 1 is present with the correct polarity in both multiple stacks. Thus, when all three stacks (i.e., *Ps*, *Pps*, and *PpSs*) are combined in a multiphase stack (Figure 4d), it is Peak 1 that is imaged and accordingly interpreted as representing the Moho as shown in Figure 4d. Hence, what was initially a region open to misinterpretation in terms of Moho depth is resolved into a single easily identifiable continuous Moho arrival through the application of the multiphase stacking technique.

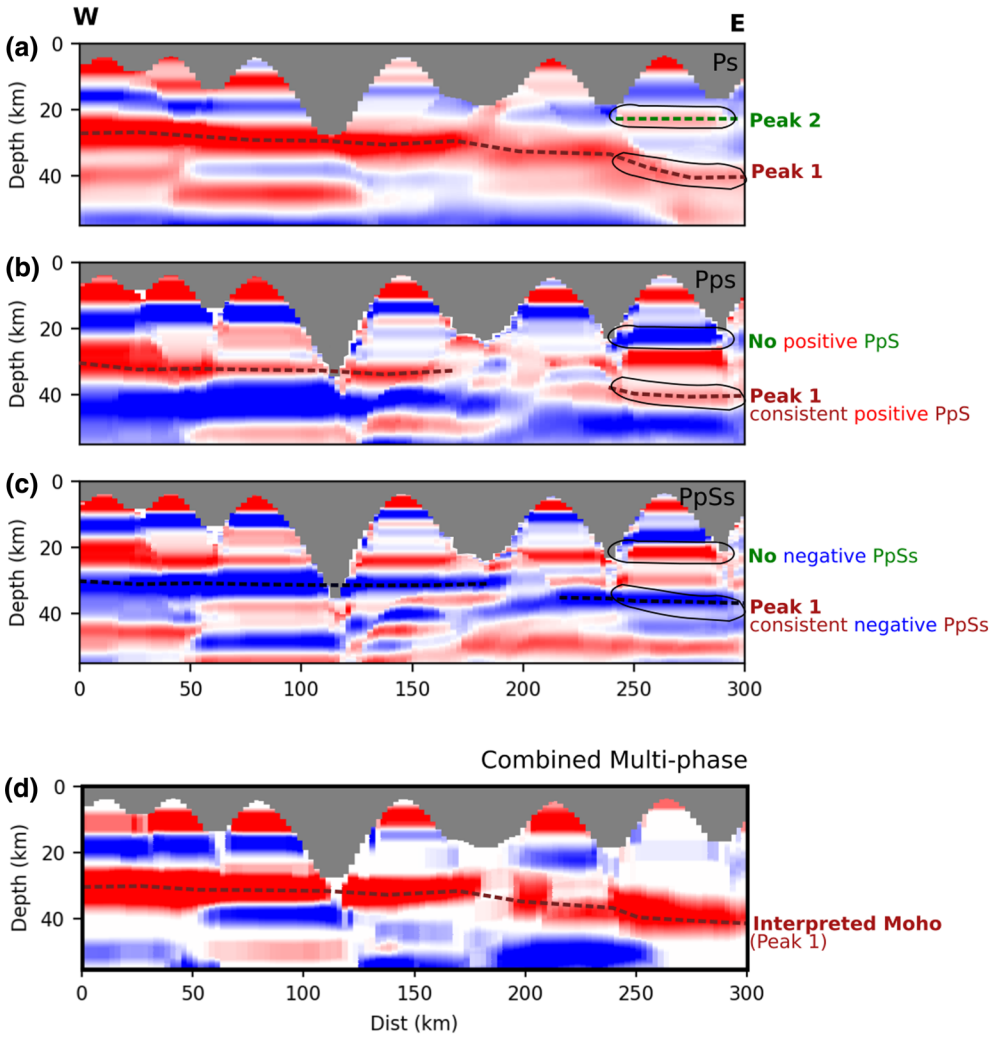

Figure 4. Example of how multiphase CCP stacks are created using RF data smoothed over 2 × ray Fresnel zones. Individual CCP stacks created for each time-depth conversion assuming all peaks represent (a) direct *Ps* converted phases, (b) *PpPs* multiples, and (c) *PpSs* multiples (which are of opposite polarity). These are combined where all three show a consistent arrival to produce (d) the final multiphase stack. The Moho arrival is highlighted with dotted lines in each stack. Profiles show the first 170 km of Rransect A-A′ in Figure 5a.

3.4. Potential Sources of Error

Here we briefly discuss potential sources of error on Moho depth measurements, how we attempt to account for them, and, where possible, quantify them:

1. Choice of velocity model: The factor which has the greatest impact on measured Moho depth is the choice of correcting velocity model. It is not possible to quantify these errors since Moho depth estimates are entirely dependent on which models are used and the inherent errors within them, which are difficult to formally assess. We attempt to address this uncertainty by exploring two different velocity models used in time-to-depth corrections and assessing the differences in resulting Moho depths (a 1-D local model, Karabulut et al., 2011, and 3-D full waveform model, Çubuk-Sabuncu et al., 2017). Differences in Moho depth observations made after applying the two models varies laterally across the study area (supporting information Figure S2). Maximum differences in Moho depths are ±7 km, but an average of differences across the whole study region is only ±1.2 km. For further discussion on the effects of velocity corrections see supporting information Text S1 and Figure S2.
2. Data noise/variability: Noisy data can lead to spurious arrivals, which are not representative of real structure. We address this issue by stacking data and only analyzing regions sampled by at least three pieces of

data and by only analyzing observed peak arrivals that are deemed statistically robust by being >2 standard error of the mean. How data variability affects measured Moho depths can be quantified using statistical methods such as bootstrapping (i.e., restacking many random subsets of data and comparing the variability in results). While this is not possible across our whole study area, we apply a small-scale test over the region sampled by the dense DANA array to the east of the Sea of Marmara, where data subsets do not drastically change the size and shape of the sampled area (see supporting information Text S2 and Figure S3 for details). Standard deviation of Moho depth estimates is <0.4 km across data subsets for the majority of the area.

3. Misinterpretation of phases: A direct Ps phase from ~40 km depth arrives at the same time and with the same polarity as a *PpPs* phase from ~10 km depth. Thus, misinterpreting a multiple phase as a true Ps conversion could cause errors on the order of tens of kilometers in Moho depth estimates. By using a multiphase stacking method, we only interpret observations that show direct arrivals and two consistent multiples, reducing the possibility of phase misinterpretation errors.

The error sources discussed are not all easily quantifiable and vary laterally across the study region. Thus, it is not possible to put meaningful error bounds on Moho depth estimates, which take into account all possible sources of error. However, due to the steps we have taken to mitigate these effects, we are confident in the robustness of our results at the regional scale.

4. Results

Results discussed in this section are derived from RFs converted from time to depth using the 3-D full waveform model of Çubuk-Sabuncu et al. (2017). All features described here are also observed after 1-D time-depth conversions, using the model of Karabulut et al. (2011). This is significant, because it demonstrates that the structures imaged are present as differences in RF phase arrival times, and not an artifact imposed by our choice of 3-D velocity model. The main differences observed after application of 3-D corrections compared to 1-D is a sharpening of identified features and smoothing out of smaller-scale Moho variations, further indicating the validity of our use of 3-D velocity corrections. For a direct comparison of 1-D and 3-D results and further discussion on the effects of velocity correction see supporting information Text S1 and Figure S2.

4.1. Regional Moho Depth Variability

The largest amplitude automatically picked peaks in CCP stacks, which relate to the most laterally continuous features observed in cross sections, are found within the depth range of 26–41 km. We interpret these arrivals as representing the seismic Moho and extract peaks to produce a new map of crustal thickness variation across the Marmara region (Figure 5). The map shows some small-scale topographic variation on the Moho, which is likely to reflect variability in the location of stacked peak maxima due to variable stacking accuracy. Accordingly, we interpret only large-scale regional features, which we deem to be more robust.

Crustal thickness varies from 26 to 41 km. There is a general thickening of the crust from average values of 30 km west of 28.5°E, to 35 km to the east. The thinnest crust (26 km) lies beneath the western side of the Sea of Marmara transtensional Tekirdag basin. An E-W cross section through this region indicates an abrupt shallowing of the Moho into this thinned region between 27.8°E and 27.6°E (Figure 5c, marked in gray on the cross section). We lack data coverage in the central Sea of Marmara and eastern limits suggest a slightly thicker crust within the Cinarcik basin south of Istanbul.

The thickest crust of up to 41 km is observed in the NE of the study region, seemingly in a distinct region bounded by the northern strand of the North Anatolian Fault to the south and the West Black Sea Fault to the west. An E-W cross section through this region of thickened crust indicates a distinct change of Moho character across the West Black Sea Fault from subhorizontal to dipping (Figure 5a).

4.2. High-Resolution Moho Map of the Eastern Sea of Marmara Region

Figure 6 shows results from the densely sampled region east of the Sea of Marmara, where increased data coverage allows the production of a CCP stack without additional smoothing where data are added over 1 × Fresnel zone of rays. The map of Moho depths confirms features identified in the smoothed

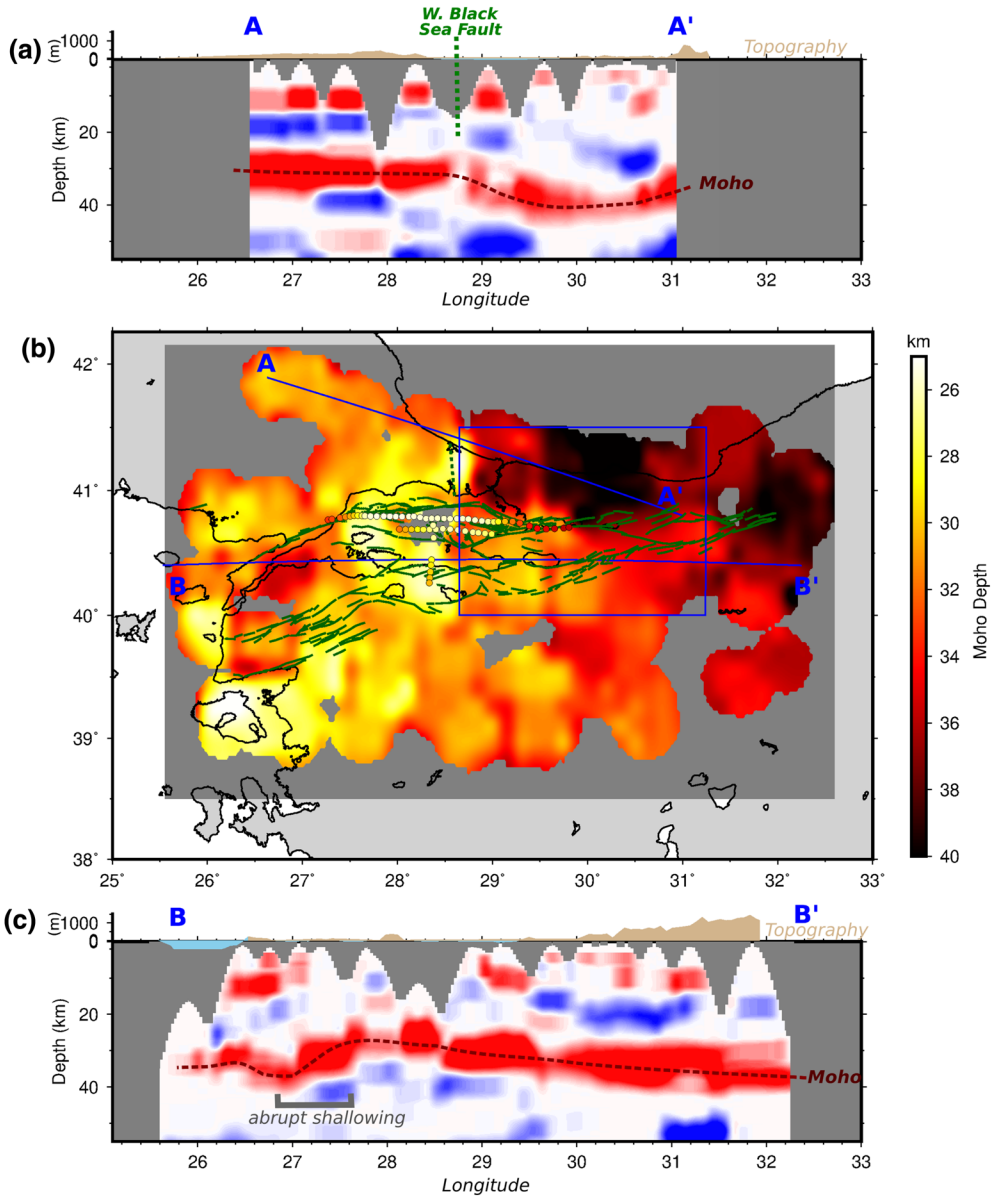

Figure 5. (a) A-A′ cross section through multiphase CCP stacked RF data. Red = positive and blue = negative amplitude arrivals. Interpreted Moho is shown with a dashed dark red line, corresponding topography at the surface is shown above. Grayed out regions are areas of no data coverage. (b) Map of Moho discontinuity depths across the study area picked from multiphase CCP stacked RF data. Colored circles show Moho depth estimates from the refraction survey of Bécel et al. (2009). Green lines show faults as described in previous figures. Blue square shows region of 1 × Fresnel zone stacks shown in Figure 6. Locations of cross sections marked with blue lines. (c) B-B′ cross section through CCP stacked data.

2 × Fresnel zone stack, of a particularly thick region of crust north of the North Anatolian Fault, with a sharp western boundary along the West Black Sea Fault.

N-S transects through this region (Figures 6b–6d) sample from south to north across the Sakarya, Armutlu-Almacik, and Istanbul crustal blocks as well as bisecting the northern and southern branches of the North Anatolian Fault. Transects show a relatively continuous Moho across the southern branch of the North Anatolian Fault. Conversely, the Moho is disrupted in various ways across the northern branch in all three cross sections: Transect 1 shows an abrupt reduction in Moho visibility (at 41° latitude), Transect 2 shows a double peaked arrival (at 40.7° latitude), and Transect 3 shows a subtle but distinct increase in depth (at 40.8° latitude), which correlates to the location of the fault trace at the surface. The double peaked structure

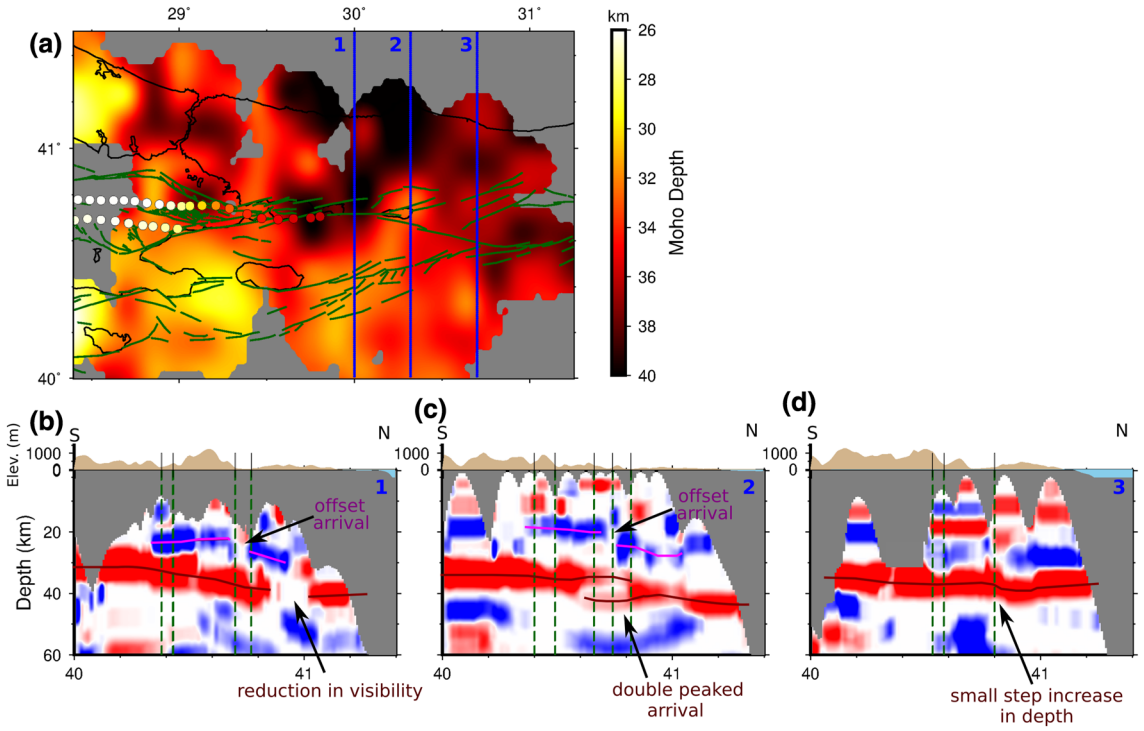

Figure 6. (a) Map of Moho discontinuity depths across the study area picked from high-resolution 1 × fres CCP stack. Colored circles show Moho depth estimates from the refraction survey of Bécel et al. (2009). (b–d) S-N cross sections through the CCP stack displayed as described in Figures 5a and 5c, with the addition of surface fault traces extrapolated to depth shown as dark green dashed lines, interpreted Moho shown highlighted by dark red lines and an interpreted disruption of a negative arrival highlighted by magenta lines.

observed in Transect 2 could be caused by a sharp step in discontinuity depth. Previous RF modeling has shown that an abrupt increase in Moho depth can set up a double peaked arrival for rays sampling across a step (Mitra et al., 2018). A double peak can also be formed as a stacking artifact where a step increase in discontinuity depth of greater than our 5 km vertical resolution becomes smoothed out across the width of the horizontally applied Fresnel zone in stacks.

We also note that more poorly imaged upper crustal discontinuities seem to be affected as they move northward across the northern fault branch. Particularly, the highlighted negative polarity arrival in Figures 6b and 6c Transects 1 and 2, which changes from being subhorizontal to dipping on either side of the fault trace, as well as showing a reduction in visibility across the fault trace itself.

5. Discussion

We produce a new map of crustal structure in the Marmara region. We observe a regional signal of gradually thickening crust from west to east, superimposed over smaller-scale thickness variations. A distinct region of thicker ~40 km crust is identified in the NE of our study region, bounded by the North Anatolian Fault to the south and the West Black Sea Fault to the west. Detailed cross sections show disruption of imaged features across the northern branch of the North Anatolian Fault.

5.1. Regional Westward Thinning Due to Western Anatolian Extension

The observation of general westward crustal thinning is consistent with a Turkey-wide signal observed in previous RF studies (Tezel et al., 2013; Vanacore et al., 2013); see supporting information Figure S6 for direct comparison of these studies with results presented here. We interpret this regional signal as reflecting the effects of the present day extensional regime within the western Anatolia and Aegean regions causing crustal thinning with a decreasing effect toward the east.

Vanacore et al. (2013) suggest the undeformed Arabian plateau in central Turkey has median crustal thicknesses of 37 km, while Saunders et al. (1998) define a value of 38 km. If these are taken to represent undeformed crustal values, then the majority of the Marmara region imaged in this study can be considered to have felt the effects of extension and thinning to varying degrees. However, the variety of crustal terranes of different tectonic origins make such a single broad interpretation difficult to apply regionally across a study region which includes much smaller-scale crustal thickness variations.

5.2. Crustal Thinning Under the Transtensional Sea of Marmara

We observe thinnest crustal measurements of 26 km beneath the western side of the Sea of Marmara, which shows a distinct thinning from 30 km to 26 km moving eastward into the Tekirdag basin. This thinning is consistent with refraction measurements (marked as colored circles in Figures 5b and 6a), which find thicknesses of 26 km within the Western High and Central basin with sharp decreases in thickness from onshore to off-shore (Bécel et al., 2009).

While refraction estimates match our RF based Moho measurements well in the central and western areas of the Sea of Marmara, in the east Moho depths based on refraction appear to be thinner by approximately 5 km than observed in our results (Figures 5b and 6a). Thus, interpretation of structure in this region should be taken with caution. Our results in this eastern region show slightly thicker crust of ~30 km, suggesting that maximum thinning does not occur until a location westward of Istanbul. If this observation is correct this increase in crustal thickness eastward throughout the Sea of Marmara would be consistent with the hypothesis that opening initiated in the west of the basin and gradually propagated toward the east. This ongoing process is exemplified by the Izmit bay (the current eastern termination of the Sea of Marmara) and the Sapanca Lake, which will likely connect to the Sea of Marmara in the future. There are also indications that the Karadere fault, even further west may be in the early stages of forming a transtensional basin (Najdahmadi et al., 2016).

In particular, unusually deep Moho depths of ~38 km are observed in the small region offshore Istanbul, just south of the Princes Islands. This region is overlain by the Cinarcik basin, which is imaged as strong slow wave speed anomalies in the top 1–4.5 km in the local seismic noise study of Acarel et al. (2014). The small length scale of this feature means it is not well imaged in the regional velocity model we use for time-to-depth corrections (Çubuk-Sabuncu et al., 2017). Slow seismic velocity anomalies that are not accounted for would map into deeper Moho depths, which may explain the deeper than expected observations in this region. Alternatively, the lateral smoothing imposed in our CCP stacks may smooth some deep Moho observations just to the north in the IZ southward into this region.

5.3. Ancient Crustal Terranes and Lithospheric Isostasy

The region of increased crustal thickness in the NE of our study region appears to define the ancient crustal terrane of the Istanbul Zone (IZ). The southern limit of the terrane, defined by the location of the northern strand of the North Anatolian Fault, has previously been shown to display a sharp increase in crustal thickness using transfer functions (Frederiksen et al., 2015). In contrast, the RF study of Kahraman et al. (2015) do not observe this sharp step increase in Moho depth over the northern branch of the North Anatolian Fault. However, they do note the appearance of a deeper arrival in this region. It is our belief that our multiphase stacking method has determined that this deeper arrival represents the Moho, rather than the shallower arrival interpreted by Kahraman et al. (2015), similar to the example situation shown in Figure 4. For a direct comparison of Moho depth estimates in our study compared to these two previous studies, see supporting information Figure S7 and Text S4.

We show this sharp increase in Moho thickness into the IZ is also observable along the extinct West Black Sea Fault, which defines the western limit of the terrane. Our observations of increased crustal thickness in the IZ are consistent with its hypothesized tectonic origin north of the Black Sea and subsequent southward translation to its current location (Okay et al., 1994). The IZ shows a distinct difference in structure compared to the rest of the Marmara region. Its imaged crustal thickness of 35–40 km is similar to that measured by refraction surveys near to its hypothesized region of origin on the Scythian platform (e.g., Starostenko et al., 2015; Yegorova et al., 2010).

We note that the thickened crust of the IZ lies in a region of low surface topography, while areas south of the Intra-Pontide suture in the Sakarya Zone have higher topography but thinner crust. Isostatic considerations

indicate that higher-elevation topography would be expected to be compensated by thicker crust. Hence, crustal thickness and elevation should positively correlate. It is therefore interesting to observe that the crust beneath the IZ is 6 km thicker than beneath the Sakarya Zone, where the topography is 0.6 km higher based on digital elevation model ETOPO1 (Amante & Eakins, 2001). This inverse relationship between Moho depth and elevation indicates that topography in this region is not compensated by differences in crustal thickness, which has been previously suggested by Frederiksen et al. (2015).

We investigate the constraints that this apparent discrepancy places on lithospheric structure in these two locations. The difference in elevation, Δe, between two lithospheric columns can be calculated using an isostatic relationship so that

$$\Delta e = \Delta t_c \left(\frac{\rho_a - \rho_c}{\rho_a}\right) + \Delta t_{lm} \left(\frac{\rho_a - \rho_{lm}}{\rho_a}\right) - (t_c + \Delta t_c)\left(\frac{\Delta \rho_c}{\rho_a}\right), \quad (3)$$

where t_c and t_{lm} are the thickness of continental crust and lithospheric mantle in the reference column (i.e., the left-hand side of Figure 7a; note that t_{lm} does not appear in Equation 3 but is shown on Figure 7a for reference); Δt_c and Δt_{lm} are the difference in crustal thickness and lithospheric mantle thickness between the two columns (i.e., left- and right-hand sides of Figure 7a); ρ_c is the density of crust in the reference column; and ρ_{lm} and ρ_a are the bulk densities of lithospheric mantle and asthenospheric mantle, which can be taken to be constant (Figure 7a).

Here we analyze the isostatic consequences of varying three parameters to explain the change in elevation between the IZ and Sakarya Zone using their measured difference in crustal thickness of $\Delta t_c = -6$ km. We use the IZ as our reference column, where $t_c = 40$ km, and we fix $\rho_a = 3.2$ Mg m^{-3} and $\rho_c = 2.8$ Mg m^{-3}. First, we fix $t_{lm} = 3.33$ Mg m^{-3} and investigate the trade-off between crustal density and lithospheric thickness differences required to produce the value of $\Delta e = 0.6$ km that is observed (i.e., the zero contour on Figure 7b). This suite of calculations indicates that either the lithosphere beneath the Sakarya Zone must be ~45 km thinner than beneath the IZ or the crust is 0.13 Mg m^{-3} lighter. Next, in order to test the effect of uncertainties in lithospheric mantle density, we hold ρ_c constant (i.e., $\Delta \rho_c = 0$ Mg m^{-3}) and instead vary the density of the lithospheric mantle, ρ_{lm} beneath both zones (Figure 7c). This test confirms that at least ~20 km of difference in lithospheric thickness is required between the two continental blocks if they are composed of crust of the same density. Our simple calculations show that for the range of reasonable values of $\Delta \rho_c$ and ρ_{lm} shown on Figures 7b and 7c, the lithospheric mantle beneath the Sakarya Zone may be a few tens of kilometers thinner than beneath the IZ unless there is a large difference in crustal density between the two regions.

We conclude that if the IZ and Sakarya Zone are both isostatically compensated within the lithosphere, then either the IZ is characterized by crust that is 0.13 Mg m^{-3} denser than the Sakarya Zone or has a lithospheric mantle which is ~20–50 km thicker. It is likely that a combination of these two factors is at play. Higher values of bulk V_p and positive short-wavelength gravity anomalies in the IZ indicate that the crust is likely to be somewhat denser. However, a difference in lithospheric thickness is consistent with the different tectonic origins of the IZ and Sakarya Zone. The IZ originated from the Odessa Shelf, to the north of the Black sea, which is characterized by thicker lithosphere of 160–200 km compared to the Anatolian lithosphere that ranges from < 100–150 km (Hoggard et al., 2020; Priestley & McKenzie, 2013, see Figure S8 in the supporting information). Our calculations suggest that the IZ has thicker lithospheric mantle than the Sakarya Zone further to the south are consistent with these observations.

This result differs from the findings of Karabulut et al. (2019) who state that the elevation of Anatolia can be explained by variations in crustal thickness alone and suggest that lower crustal flow has smoothed out changes in crustal structure across component continental fragments, though they do note that exceptions may be found in the Pontides. This conclusion is based on similar observations to our own, by comparing crustal thickness estimates from RF measurements to topographic elevation. The small lateral extent of the IZ that we are able to image with our comprehensive regional dataset is likely to be below the lateral resolution of the more distributed dataset of Karabulut et al. (2019).

Finally, we note that several authors have previously argued that some component of Anatolian topography has grown since Neogene times as a result of changes in the pattern of subplate mantle convection (e.g.,

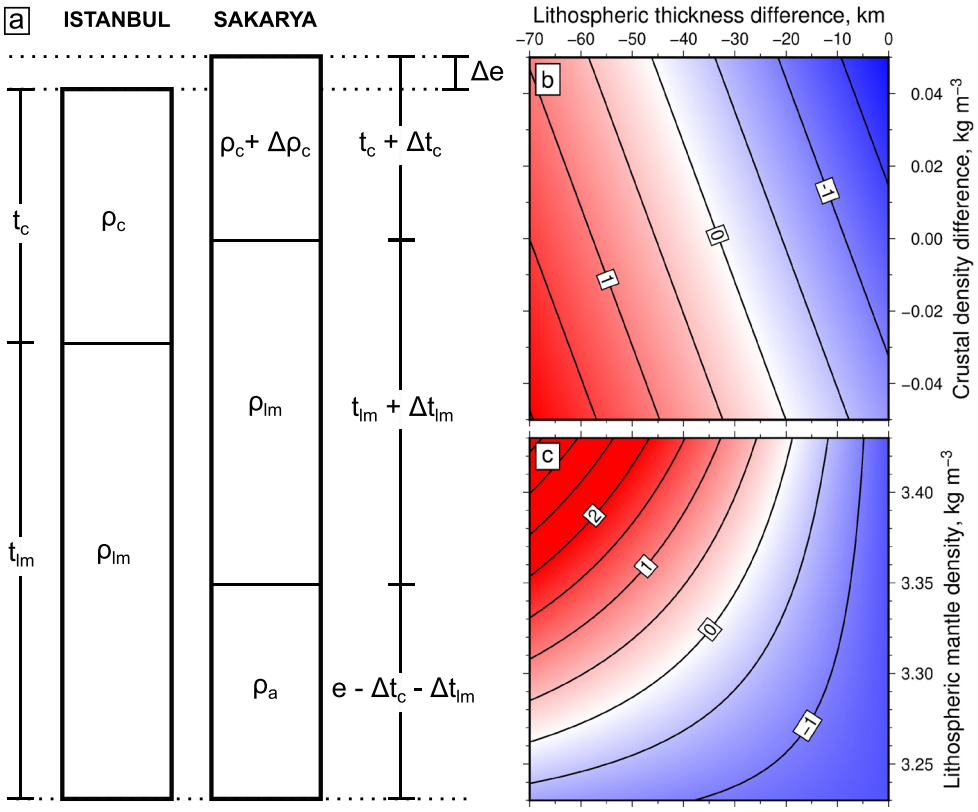

Figure 7. Elevation estimates from isostatic calculations. (a) Cartoons showing two continental columns used in isostatic calculations. (b) Difference between observed and calculated elevation change between region of thick and thin crust as function of lithospheric thickness difference and crustal density difference. t_c=40 km, ρ_c=2.8 Mg m^{-3}, ρ_a=3.2 kg M^{-3}, ρ_{lm}=3.33 Mg m^{-3}, Δt_c=−6 km, observed elevation difference, Δe=0.6 km. Red (blue) colors = over (under) estimate. (c) Difference between observed and calculated elevation change between region of thick and thin crust as function of lithospheric thickness difference and lithospheric mantle density. Parameters as for panel (b), except for constant crustal thickness of ρ_c=2,800 kg m^{-3} (i.e., $\Delta\rho_c$=0 kg m^{-3}).

Faccenna & Becker, 2010; Faccenna et al., 2014; McNab et al., 2018; Şengül Uluocak et al., 2016). Mantle convective processes are likely to be expressed as broad topographic swells of ≥ 1,000 km wavelengths and so differences in convective support between the Sakarya and IZs are likely to be small, suggesting that topographic differences are compensated lithospherically.

5.4. Effect of Present-Day Deformation Along the North Anatolian Fault

Cross sections through the northern and southern branches of the North Anatolian Fault west of the Sea of Marmara (Figures 6b–6d) seem to show continuous crustal features across the southern branch and disruption of structure across the northern branch.

Similar observations of structural disruption have been imaged by local studies using both RF (Kahraman et al., 2015) and ambient noise auto-correlations (Taylor et al., 2016). Such observations indicate localized shear along the northern North Anatolian Fault branch extends deep into the crust and potentially into the upper mantle, while the lack of such observations across the southern branch indicates less strain accumulation. This interpretation is consistent with the observation that the majority of slip is accommodated on the northern rather than southern branch (McClusky et al., 2000; Reilinger et al., 2006). However, as discussed in the previous section, the northern branch also defines a change in crustal terrane into the Istanbul block, which is of distinctly different origin. Thus, it could be that changes in features across the northern branch simply represent a change in crustal structure between terranes.

Deformation along the present-day fault, and the associated fault damage zone, would be expected to reduce reflectivity of discontinuities in the vicinity of the fault (Taylor et al., 2016). We see a clear reduction in visibility of a negative polarity arrival at ~20 km depth (Figures 6b and 6c, Sections 1 and 2), coincident with the

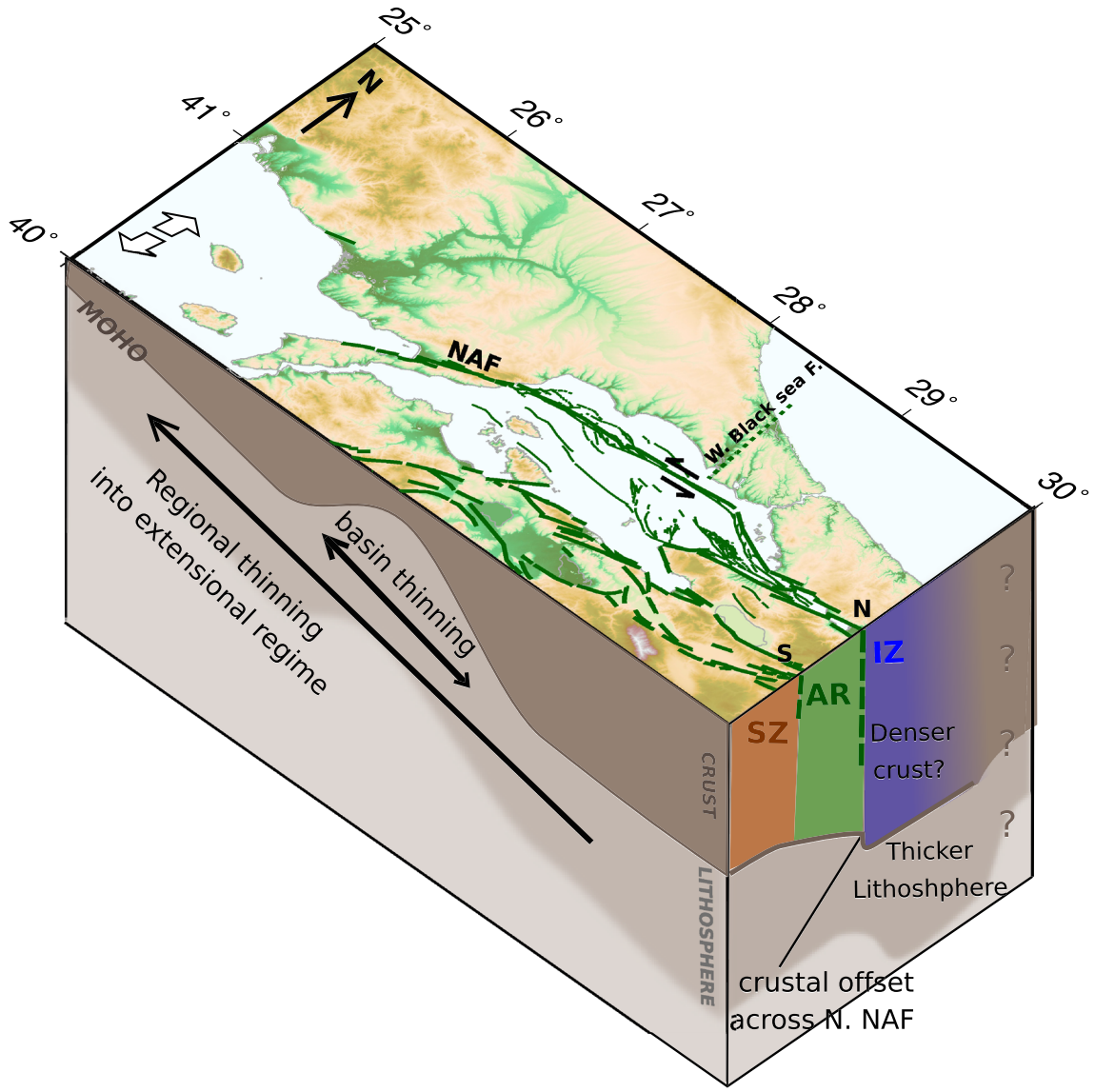

Figure 8. Summary cartoon of the crustal structure imaged in this study. Faults plotted in green as shown in Figure 1b. SZ = Sakarya Zone, IZ = Istanbul Zone, and AR = Armutlu-Almacik block, NAZ = North Anatolian Fault.

fault trace at the surface. We interpret this decrease in amplitude to indicate that localized strain accumulation on the northern branch extends to at least 20 km depth, if not deeper. The correlation with surface fault traces indicates a near-vertical fault at depth. This contradicts the suggestion made by Kahraman et al. (2015), of a change from a near vertical orientated fault at ~30.2°E to a 60° northward dip on both faults strands further eastward at ~30.5°E (between Sections 2 and 3 in Figures 6c and 6d). We do observe a reduction in Moho amplitude offset northward on Section 1 in Figure 6. However, this is further westward (30°E) away from the region of predicted dipping structures of Kahraman et al. (2015), and there is clear disruption of a negative arrival directly beneath the surface fault trace at 20 km depth. Thus, we do not find any evidence of significant dip to fault structures.

6. Conclusions

We present a new map of regional crustal thickness variations across the Marmara region of northwestern Turkey. Complex variations in crustal structure reflect both modern active tectonic processes across a range of scales, as well as variation in the ancient crustal terrane fragments which form the region.

Major interpreted features (as depicted in Figure 8) include the following:

- A regional signal of westward crustal thinning, due to the effect of the trench rollback-driven extension in western Anatolia and the Aegean region.
- Observations of the thinnest crust (up to 26 km) are found in the western Sea of Marmara, reflecting the local effects of transtensional basin opening, which appears to be further developed in the west compared to the east.
- A region of increased crustal thickness of ~40 km, with sharp boundaries delineated by the northern branch of the North Anatolian Fault and the extinct West Black Sea Fault, which is interpreted as representing the ancient crustal terrane of the Istanbul Zone (IZ).
- The IZ's thick crust and low topography suggest it is not in crustal isostatic equilibrium, probably due to loading by thicker lithospheric mantle.
- Disruption of imaged discontinuity structure across the northern branch of the North Anatolian Fault to the east of the Sea of Marmara indicates localized strain extends to depths of at least 20 km if not deeper, solely along the more active northern branch.

The crustal thickness observations we present here are regionally continuous and methodologically consistent and incorporate the most up to date models of velocity structure in the region. For this reason we hope that this new map of crustal thickness will prove a useful resource for future studies analyzing the Marmara region.

Data Availability Statement

This study uses Obspy (Krischer et al., 2015). Data are retrieved from IRIS DMC (www.iris.edu) from networks: KO, YH, YI, XY, XW, HL, and HT. Moho measurements are available in the supporting information.

Acknowledgments

We would like to acknowledge Dr. Heiko Worth for providing data from the ARNET seismic network. J. J. was partially supported by the European Research Council (ERC) under the European Union's Horizon 2020 research and innovation programme (Grant Agreement 804071 - ZoomDeep). P. M. G acknowledges funding from Helmholtz Young Investigators Group SAIDAN (VH-NG-1323). S. S. is funded by BP under Participation Agreement R28596/CN001.

References

Acarel, D., Bulut, F., & Bohnhoff, M. (2014). Ambient noise analysis in the eastern sea of Marmara region in northwest Turkey: Lateral variations of the crustal velocity field. *Bulletin of the Seismological Society of America*, *104*(4), 1954–1963.

Amante, C., & Eakins, B. W. (2001). ETOPO1 1 arc-minute global relief model: Procedures, data sources and analysis. National Geophysical Data Center, NOAA. https://doi.org/10.7289/V5C8276M

Aristotle University of Thessaloniki, Seismological Network (1981). Permanent Regional Seismological Network operated by the Aristotle University of Thessaloniki. International Federation of Digital Seismograph Networks. Other/Seismic Network. https://doi.org/10.7914/SN/HT

Armijo, R., Pondard, N., Meyer, B., Uçarkus, G., de Lépinay, B. M., Malavieille, J., et al. (2005). Submarine fault scarps in the sea of Marmara pull-apart (North Anatolian Fault): Implications for seismic hazard in Istanbul. *Geochemistry, Geophysics, Geosystems*, *6*, Q06009. https://doi.org/10.1029/2004GC000896

Barka, A. A. (1992). The North Anatolian fault zone. In *Annales tectonicae*, *6*, pp. 164–195.

Bécel, A., Laigle, M., de Voogd, B., Hirn, A., Taymaz, T., Galvé, A., et al. (2009). Moho, crustal architecture and deep deformation under the north Marmara trough, from the SEISMarmara leg 1 offshore–onshore reflection–refraction survey. *Tectonophysics*, *467*(1-4), 1–21.

Ben-Zion, Y., & Lyakhovsky, V. (2002). Accelerated seismic release and related aspects of seismicity patterns on earthquake faults, *Earthquake processes: Physical modelling, numerical simulation and data analysis Part II* (pp. 2385–2412): Springer.

Bird, P. (2003). An updated digital model of plate boundaries. *Geochemistry, Geophysics, Geosystems*, *4*(3), 1027. https://doi.org/10.1029/2001GC000252

Bohnhoff, M., Bulut, F., Dresen, G., Malin, P. E., Eken, T., & Aktar, M. (2013). An earthquake gap south of Istanbul. *Nature Communications*, *4*, 1999.

Bohnhoff, M., Harjes, H.-P., & Meier, T. (2005). Deformation and stress regimes in the Hellenic subduction zone from focal mechanisms. *Journal of Seismology*, *9*(3), 341–366.

Bohnhoff, M., Martínez-Garzón, P., Bulut, F., Stierle, E., & Ben-Zion, Y. (2016). Maximum earthquake magnitudes along different sections of the North Anatolian Fault zone. *Tectonophysics*, *674*, 147–165.

Bohnhoff, M., Wollin, C., Domigall, D., Küperkoch, L., Martínez-Garzón, P., Kwiatek, G., et al. (2017). Repeating Marmara Sea earthquakes: Indication for fault creep. *Geophysical Journal International*, *210*(1), 332–339.

Bulut, F., Bohnhoff, M., Aktar, M., & Dresen, G. (2007). Characterization of aftershock-fault plane orientations of the 1999 izmit (Turkey) earthquake using high-resolution aftershock locations. *Geophysical Research Letters*, *34*, L20306. https://doi.org/10.1029/2007GL031154

Bulut, F., Bohnhoff, M., Eken, T., Janssen, C., Kılıç, T., & Dresen, G. (2012). The east Anatolian fault zone: Seismotectonic setting and spatiotemporal characteristics of seismicity based on precise earthquake locations. *Journal of Geophysical Research*, *117*, B07304. https://doi.org/10.1029/2011JB008966

Bulut, F., Bohnhoff, M., Ellsworth, W. L., Aktar, M., & Dresen, G. (2009). Microseismicity at the North Anatolian fault in the Sea of Marmara offshore Istanbul, NW Turkey. *Journal of Geophysical Research*, *114*, B09302. https://doi.org/10.1029/2008JB006244

Çubuk-Sabuncu, Y., Taymaz, T., & Fichtner, A. (2017). 3-D crustal velocity structure of western Turkey: Constraints from full-waveform tomography. *Physics of the Earth and Planetary Interiors*, *270*, 90–112.

DANA (2012). Dense array for North Anatolia. Dataset/Seismic Network. https://doi.org/10.7914/SN/YH_2012

Elmas, A. (2012). The Thrace basin: Stratigraphic and tectonic-palaeogeographic evolution of the palaeogene formations of northwest Turkey. *International Geology Review*, *54*(12), 1419–1442.

Elmas, A., & Yiğitbaş, E. (2001). Ophiolite emplacement by strike-slip tectonics between the Pontide zone and the Sakarya zone in northwestern Anatolia, Turkey. *International Journal of Earth Sciences*, *90*(2), 257–269.
England, P., Houseman, G., & Nocquet, J.-M. (2016). Constraints from GPS measurements on the dynamics of deformation in Anatolia and the Aegean. *Journal of Geophysical Research: Solid Earth*, *121*, 8888–8916. https://doi.org/10.1002/2016JB013382
Ergintav, S., Reilinger, R. E., Çakmak, R., Floyd, M., Cakir, Z., Doğan, U., et al. (2014). Istanbul's earthquake hot spots: Geodetic constraints on strain accumulation along faults in the Marmara seismic gap. *Geophysical Research Letters*, *41*, 5783–5788. https://doi.org/10.1002/2014GL060985
Faccenna, C., & Becker, T. W. (2010). Shaping mobile belts by small-scale convection. *Nature*, *465*(7298), 602.
Faccenna, C., Becker, T. W., Auer, L., Billi, A., Boschi, L., Brun, J. P., et al. (2014). Mantle dynamics in the Mediterranean. *Reviews of Geophysics*, *52*, 283–332. https://doi.org/10.1002/2013RG000444
Faccenna, C., Bellier, O., Martinod, J., Piromallo, C., & Regard, V. (2006). Slab detachment beneath eastern Anatolia: A possible cause for the formation of the north Anatolian fault. *Earth and Planetary Science Letters*, *242*(1-2), 85–97.
Flerit, F., Armijo, R., King, G., & Meyer, B. (2004). The mechanical interaction between the propagating north Anatolian fault and the back-arc extension in the aegean. *Earth and Planetary Science Letters*, *224*(3-4), 347–362.
Frederiksen, A. W., Thompson, D. A., Rost, S., Cornwell, D. G., Gülen, L., Houseman, G. A., et al. (2015). Crustal thickness variations and isostatic disequilibrium across the north Anatolian fault, western Turkey. *Geophysical Research Letters*, *42*, 751–757. https://doi.org/10.1002/2014GL062401
Görür, N., & Okay, A. A. (1996). A fore-arc origin for the thrace basin, NW Turkey. *Geologische Rundschau*, *85*(4), 662–668.
Hergert, T., & Heidbach, O. (2011). Geomechanical model of the Marmara sea region II. 3-D contemporary background stress field. *Geophysical Journal International*, *185*(3), 1090–1102.
Hoggard, M. J., Czarnota, K., Richards, F. D., Huston, D. L., Jaques, A. L., & Ghelichkhan, S.(2020). Global distribution of sediment-hosted metals controlled by craton edge stability. *Nature Geoscience*, *13*. https://doi.org/10.31223/osf.io/2kjvc
Jenkins, J., Maclennan, J., Green, R. G., Cottaar, S., Deuss, A. F., & White, R. S. (2018). Crustal formation on a spreading ridge above a mantle plume: Receiver function imaging of the icelandic crust. *Journal of Geophysical Research: Solid Earth*, *123*, 5190–5208. https://doi.org/10.1029/2017JB015121
Kahraman, M., Cornwell, D. G., Thompson, D. A., Rost, S., Houseman, G. A., Türkelli, N., et al. (2015). Crustal-scale shear zones and heterogeneous structure beneath the north Anatolian fault zone, Turkey, revealed by a high-density seismometer array. *Earth and Planetary Science Letters*, *430*, 129–139.
Kandilli Observatory and Earthquake Research Institute, Bosphorus Univ (2001). Bogazici University Kandilli Observatory and Earthquake Research Institute,. Dataset/Seismic Network. https://doi.org/10.7914/SN/KO
Karabulut, H., Paul, A., Özbakir, A. D., Ergün, T., & Şentürk, S. (2019). A new crustal model of the Anatolia–aegean domain: Evidence for the dominant role of isostasy in the support of the Anatolian plateau. *Geophysical Journal International*, *218*(1), 57–73.
Karabulut, H., Schmittbuhl, J., Özalaybey, S., Lengline, O., Kömeç-Mutlu, A., Durand, V., et al. (2011). Evolution of the seismicity in the eastern Marmara sea a decade before and after the 17 August 1999 Izmit earthquake. *Tectonophysics*, *510*(1-2), 17–27.
Klinger, Y. (2010). Relation between continental strike-slip earthquake segmentation and thickness of the crust. *Journal of Geophysical Research*, *115*, B07306. https://doi.org/10.1029/2009JB006550
Krischer, L., Megies, T., Barsch, R., Beyreuther, M., Lecocq, T., Caudron, C., & Wassermann, J. (2015). ObsPy: A bridge for seismology into the scientific python ecosystem. *Computational Science & Discovery*, *8*(1), 014003.
Le Pichon, X., Şengör, A. M. C., Kende, J., İmren, C., Henry, P., Grall, C., & Karabulut, H.(2015). Propagation of a strike-slip plate boundary within an extensional environment: The westward propagation of the north Anatolian fault. *Canadian Journal of Earth Sciences*, *53*(11), 1416–1439.
Ligorria, J. P., & Ammon, C. J. (1999). Iterative deconvolution and receiver-function estimation. *Bulletin of the Seismological Society of America*, *89*(5), 1395–1400.
Martínez-Garzón, P., Bohnhoff, M., Mencin, D., Kwiatek, G., Dresen, G., Hodgkinson, K., et al. (2019). Slow strain release along the eastern Marmara region offshore Istanbul in conjunction with enhanced local seismic moment release. *Earth and Planetary Science Letters*, *510*, 209–218.
McClusky, S., Balassanian, S., Barka, A., Demir, C., Ergintav, S., Georgiev, I., et al. (2000). Global positioning system constraints on plate kinematics and dynamics in the eastern Mediterranean and Caucasus. *Journal of Geophysical Research*, *105*(B3), 5695–5719.
McNab, F., Ball, P. W., Hoggard, M. J., & White, N. J. (2018). Neogene uplift and magmatism of Anatolia: Insights from drainage analysis and basaltic geochemistry. *Geochemistry, Geophysics, Geosystems*, *19*, 175–213. https://doi.org/10.1002/2017GC007251
Mitra, S., Priestley, K. F., Borah, K., & Gaur, V. K. (2018). Crustal structure and evolution of the Eastern Himalayan plate boundary system, northeast India. *Journal of Geophysical Research: Solid Earth*, *123*, 621–640. https://doi.org/10.1002/2017JB014714
Najdahmadi, B., Bohnhoff, M., & Ben-Zion, Y. (2016). Bimaterial interfaces at the Karadere segment of the North Anatolian fault, north-western Turkey. *Journal of Geophysical Research: Solid Earth*, *121*, 931–950. https://doi.org/10.1002/2015JB012601
National Observatory Of Athens, I. O. G. (1997). National Observatory of Athens Seismic Network. International Federation of Digital Seismograph Networks. https://doi.org/10.7914/SN/HL
Ogden, C. S., Bastow, I. D., Gilligan, A., & Rondenay, S. (2019). A reappraisal of the h–κ stacking technique: Implications for global crustal structure. *Geophysical Journal International*, *219*(3), 1491–1513.
Okay, A. I. (2008). Geology of Turkey: A synopsis. *Anschnitt*, *21*, 19–42.
Okay, A. I., Celal Sengor, A. M., & Grr, N. (1994). Kinematic history of the opening of the black sea and its effect on the surrounding regions. *Geology*, *22*(3), 267–270.
Okay, A. I., & Tüysüz, O. (1999). Tethyan sutures of northern Turkey. *Geological Society, London, Special Publications*, *156*(1), 475–515.
Paul, KHRESIF (1981). Seismic network YI:SIMBAAD temporary experiment—Anatolia eastern transect (RESIF-SISMOB), Dataset/Seismic Network. https://doi.org/10.15778/RESIF.YI2008
Paul, KHRESIF (2007). Seismic network XW:SIMBAAD temporary experiment—Anatolia western transect (RESIF-SISMOB). RESIF - Rseau Sismologique et godsique Franais, Dataset/Seismic Network. https://doi.org/10.15778/RESIF.XW2007
Paul, KHRESIF (2013). Seismic network XY:SIMBAAD temporary experiment—Backbone of broadband stations. RESIF - Rseau Sismologique et godsique Franais, Dataset/Seismic Network. https://doi.org/10.15778/RESIF.XY2007
Priestley, K., & McKenzie, D. (2013). The relationship between shear wave velocity, temperature, attenuation and viscosity in the shallow part of the mantle. *Earth and Planetary Science Letters*, *381*, 78–91.

Pucci, S., Palyvos, N., Zabci, C., Pantosti, D., & Barchi, M. (2006). Coseismic ruptures and tectonic landforms along the Düzce segment of the North Anatolian Fault Zone (Ms 7.1, November 1999). *Journal of Geophysical Research*, *111*, B06312. https://doi.org/10.1029/2004JB003578

Reilinger, R., McClusky, S., Vernant, P., Lawrence, S., Ergintav, S., Cakmak, R., et al. (2006). GPS constraints on continental deformation in the Africa-Arabia-Eurasia continental collision zone and implications for the dynamics of plate interactions. *Journal of Geophysical Research*, *111*, B05411. https://doi.org/10.1029/2005JB004051

Saunders, P., Priestley, K., & Taymaz, T. (1998). Variations in the crustal structure beneath western Turkey. *Geophysical Journal International*, *134*(2), 373–389.

Şengör, A. M. C., Tüysüz, O., Imren, C., Sakınç, M., Eyidoğan, H., Görür, N., et al. (2005). The North Anatolian fault: A new look. *Annual Review of Earth and Planetary Sciences*, *33*, 37–112.

Şengül Uluocak, E., Pysklywec, R., & Göğüş, O. H. (2016). Present-day dynamic and residual topography in central Anatolia. *Geophysical Journal International*, *206*(3), 1515–1525.

Starostenko, V., Janik, T., Yegorova, T., Farfuliak, L., Czuba, W., Środa, P., et al. (2015). Seismic model of the crust and upper mantle in the scythian platform: The DOBRE-5 profile across the north western Black Sea and the Crimean Peninsula. *Geophysical Journal International*, *201*(1), 406–428.

Taylor, G., Rost, S., & Houseman, G. (2016). Crustal imaging across the north Anatolian fault zone from the autocorrelation of ambient seismic noise. *Geophysical Research Letters*, *43*, 2502–2509. https://doi.org/10.1002/2016GL067715

Tezel, T., Shibutani, T., & Kaypak, B. (2013). Crustal thickness of Turkey determined by receiver function. *Journal of Asian Earth Sciences*, *75*, 36–45.

Tunc, B., Caka, D., Irmak, T. S., Woith, H., Tunc, S., Baris, S., et al. (2011). The Armutlu network: An investigation into the seismotectonic setting of Armutlu–Yalova–Gemlik and the surrounding regions. *Annals of Geophysics*, *54*(1), 35–45.

Vanacore, E. A., Taymaz, T., & Saygin, E. (2013). Moho structure of the Anatolian plate from receiver function analysis. *Geophysical Journal International*, *193*(1), 329–337.

Wollin, C., Bohnhoff, M., Martínez-Garzón, P., Küperkoch, L., & Raub, C. (2018). A unified earthquake catalogue for the sea of Marmara region, Turkey, based on automatized phase picking and travel-time inversion: Seismotectonic implications. *Tectonophysics*, *747*, 416–444.

Yegorova, T., Baranova, E., & Omelchenko, V. (2010). The crustal structure of the black sea from the reinterpretation of deep seismic sounding data acquired in the 1960s. *Geological Society, London, Special Publications*, *340*(1), 43–56.

Yiğitbaş, E., Elmas, A., & Yïlmaz, Y. (1999). Pre-Cenozoic tectono-stratigraphic components of the western pontides and their geological evolution. *Geological Journal*, *34*(1-2), 55–74.

Zhu, L., & Kanamori, H. (2000). Moho depth variation in Southern California from teleseismic receiver functions. *Journal of Geophysical Research*, *105*(B2), 2969–2980.